LASER INTERFEROMETER GRAVITATIONAL WAVE OBSERVATORY
- LIGO -
CALIFORNIA INSTITUTE OF TECHNOLOGY
MASSACHUSETTS INSTITUTE OF TECHNOLOGY

Technical Note **LIGO-T1300683–v1** 2013/09/09

Tidal Prediction and Compensation in aLIGO

Final Report

Noah Kurinsky
Mentor: Kiwamu Izumi
Tufts University, LIGO Hanford Observatory

California Institute of Technology
LIGO Project, MS 18-34
Pasadena, CA 91125
Phone (626) 395-2129
Fax (626) 304-9834
E-mail: info@ligo.caltech.edu

Massachusetts Institute of Technology
LIGO Project, Room NW22-295
Cambridge, MA 02139
Phone (617) 253-4824
Fax (617) 253-7014
E-mail: info@ligo.mit.edu

LIGO Hanford Observatory
Route 10, Mile Marker 2
Richland, WA 99352
Phone (509) 372-8106
Fax (509) 372-8137
E-mail: info@ligo.caltech.edu

LIGO Livingston Observatory
19100 LIGO Lane
Livingston, LA 70754
Phone (225) 686-3100
Fax (225) 686-7189
E-mail: info@ligo.caltech.edu

`http://www.ligo.caltech.edu/`

Abstract

The solid earth tides, deformations in the Earths shape due to tidal forces from the moon and sun, cause the arms of the aLIGO interferometers to be deformed by up to 200 microns over the course of a day, which far exceeds the locking condition of less than one nanometer of longitudinal deformation. We have developed a program which can predict the deformation introduced into the arms at any point in time, and have used these predictions to propose modifications to the existing length control scheme, such that tidal effects may be reliably removed without prior knowledge of their strength at a given time. We have also integrated the prediction program into the control system such that tidal predictions may be monitored in real time, or checked to determine whether they have affected the stability of the interferometer. Herein, I also describe some future efforts that should be undertaken to improve prediction accuracy, that may be performed at a more advanced commissioning stage.

1 Introduction

Gravitational waves, spacetime ripples caused by accelerating of mass, are incredibly weak phenomena (as compared to their electromagnetic counterparts), with even the strongest signals creating local space-time strains many orders of magnitude smaller than the radius of an atom[1]. Experiments which aim to detect such small effects thus entail the development of the most sensitive instruments ever conceived by humanity, and have triggered studies of a wide variety of noise sources which are normally too weak to affect the precision of other detectors, such as small tremors caused by ocean tides or quantum laser fluctuation effects.

The Laser Interferometer Gravitational Wave Observatory (LIGO[2]) and sister projects VIRGO and GEO have attempted to reach the sensitivities required to detect gravitational waves by constructing the largest interferometers ever conceived; whereas Michelson and Morely were able to conduct their experiment in a basement, these interferometers sit on many square kilometers, with the arms of the LIGO interferometers reaching 4 km[3].

Over the past 20 years, the LIGO interferometers have gone through multiple stages of commissioning, testing, and operation, and despite impressive sensitivity achievements have yet to achieve a single confirmed gravitational wave detection. The Advanced LIGO (aLIGO) project represents the second major update of the LIGO detectors, and if successful will finally achieve sensitivities at which gravitational wave detection is a probabilistic certainty[4]. If aLIGO fails to observe the predicted level of gravitational wave events despite attaining its sensitivity goals, this will point an as-yet unseen problem with Einstein's general relativistic framework, as opposed to an experimental inadequacy.

The sensitivity requirements of gravitational wave detectors have required the development of some of the most advanced noise reduction and isolation systems ever devised, and each successive generation adopts more impressive hardware to decrease the amount of noise which can couple to the interferometer signals. The development of this hardware, and the related control systems, has entailed the study and modeling of all sorts of noise sources, and requires precision knowledge of phenomena irrelevant to less sensitive or less extended experiments.

The solid earth tides represent one of the largest sources of noise in terms of magnitude which must be considered to ensure long-term interferometer stability. Whereas a strong gravitational wave might produce a deformation in our detector on the order of 10^{-17} meters (10^{-2} fm)[1], tidal deformations can have peak to peak magnitudes on the order of around 10^{-4} m over a twelve hour time period[5]. While these effects may be separated through frequency domain analysis (the gravitational waves under study in our detector occur with frequencies between 1 and 1000 Hz), such large drifts in the interferometer arms would quickly destroy the sensitivity of the interferometer to any signal. In order for the interferometer to resonate, both arms must maintain a length equal to an integer number of laser wavelengths, and using an infrared laser, this means the arm can only be deformed by fractions of a nanometer (10^{-9} m) and still maintain a usable fraction of its maximum sensitivity[6].

The redeeming quality of the earth tides is that they are regular and fairly simple to model, and could in principle be removed from the interferometer by counteracting the predicted effects, in a method called feed-forward subtraction[7]. The purpose of this paper is to describe such a model, present the development of a program built to simulate these earth tides, and discuss whether such a feed-forward mechanism is strictly required in aLIGO, or whether we can create an adequate feedback mechanism to remove tidal effects without the use of predictions. In addition, I discuss future efforts which will be required to implement the changes I suggest herein.

2 The Effect of Earth Tides on the aLIGO Interferometers

Following from the introduction, the natural first step of any aLIGO noise analysis is to develop and test a model for the noise derived from first principles. The effect of the earth tides on our interferometers has been previously studied in by Raab and Fine[5] and Morganson[8], however I have included in this analysis an additional, parallel model to the one presented there, based on the same general theory discussed in Melchior[9] and Agnew[10].

In addition, I have verified and in some cases expanded the previous models, analyzing the assumption made and commenting on them as they arise. In this section I describe the theory and LIGO specific computation methods, and discuss the prediction program used to generate the tidal signals I use to analyze the effect of the tides on the aLIGO control systems. I additionally discuss the integration of this program into the exiting control system structure for ease of future use and analysis.

2.1 Tidal Potential

We obtain a functional form for the tidal potential by projecting the geometric potential (defined in a relatively simple manner from figure 1) into the space of spherical harmonics[10]. We can then eliminate the first two terms in the resulting sum, due to the first term being a constant (giving rise to no force) and the second term being the orbital force. The third (n=2) term is thus the dominant tidal component of the gravitational force due to additional $\frac{r}{d}$ terms, where in our case r is always $<< d$. This results in the following potential:

$$W(A) = D\left(\frac{r}{a}\right)^2\left(\frac{\langle d\rangle}{d}\right)^3\Big[\cos^2\theta\cos^2\delta\cos 2H + \sin 2\theta\sin 2\delta\cos H + 3\Big(\sin^2\theta - 1/3\Big)\Big(\sin^2\delta - 1/3\Big)\Big]$$

where $\langle d\rangle$ is the average object distance, ϕ and λ are the latitude angle and longitude respectively, $\theta = 90 - \phi$ is the colatitude of the site, and δ is the declination of the external body (as seen in

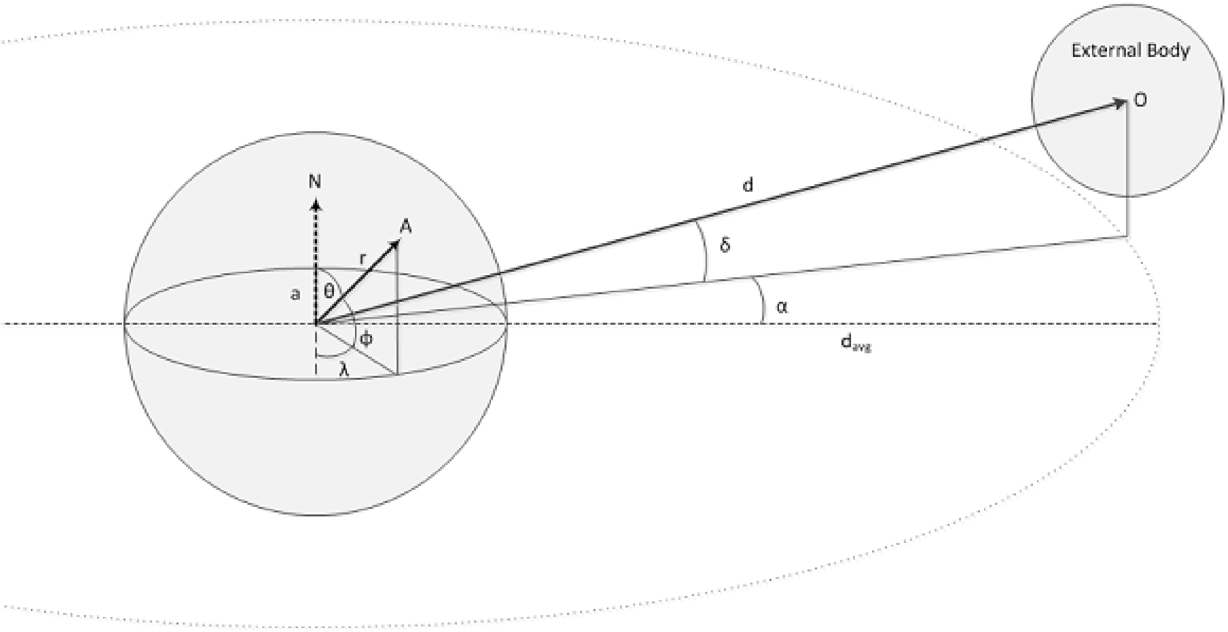

Figure 1: Model of the three-dimensional system we use to calculate tidal deformations, with separate geocentric coordinates for both the site and the body.

figure 1). The two other terms found here are Doodson's constant, defined as

$$D = \frac{3}{4} G M_{body} \frac{a^2}{\langle d \rangle^3}$$

and the local hour angle, defined as

$$H(t') = \omega t' - \alpha - \lambda$$

where ω is the sidereal velocity of the earth, t' is the sidereal time, and α is the right ascension of the body[5;9]. For a more in depth derivation, I refer the reader to Melchior[9]; Agnew[10]. For an in depth discussion of the terms of this potential, please see Kurinsky[11].

The main features to note before working with this potential are the time dependencies. We see two explicit sinusoidal variations with respect to time of day, and one term which is in principle constant. If the external bodies were stationary we would be able to ignore the constant term when considering changing potential, as we do, and simply calculate the magnitude of each potential component once.

However, the orbit of the moon about the earth and the orbit of the earth around the sun, combined with the tilt of earth's rotational axis, means these terms do vary with a time dependence related to these two cycles; explicitly we should see twice monthly and twice yearly patterns at the very least, and at times the moon and sun may cancel while at other times they may reinforce each other. For this reason, in prediction we employ highly accurate position data for all external bodies, as will be discussed in section 3.1. These frequency components are of course only important on timescales of a few days or more, however if we expect to be able to lock the aLIGO interferometers for days at a time they are nonetheless non-negligible, and they also affect the overall magnitude of the tidal effect on a given date.

2.2 Love Parameterization

In order to employ our functional potential to predict solid earth tides, we must adopt a model which relates the shape of the tidal potential to the earth deformation. Following the prevailing literature, we adopt the parameterization of E.H. Love, and describe the earth as a solid, isotropic, elastic solid, whose shape can be related to the potential by two dimension parameters l and h which we call love numbers according to the following formulae:

$$u_r = h\frac{W(A)}{g}, \quad u_\theta = \frac{l}{g}\frac{\partial W(A)}{\partial \theta}, \quad u_\phi = \frac{l}{g\sin(\theta)}\frac{\partial W(A)}{\partial \lambda}$$

where the variables are as defined in the potential, g is the gravitational acceleration at $r \approx a$, and l and h are in the range (0,1], with typical values $h \approx 0.6$ and $l \approx 0.08$[9].

From this parameterization we thus have a way to compute deformation of earth's shape in physically useful quantities. From these equations, we can then compute the deformation of each arm of the LIGO interferometers, either by displacing the ends of the arms and measuring length differentials, or by projecting tidal strains along each arm.

2.3 Displacement Method

The displacement method is the simplest conceptual extension of the Love parameterization to calculate differential length, and requires multiple steps in order to compute only deformation along the longitudinal axis of a given interferometer arm. For computational compatibility with the strain method, discussed in the next section, the implementation of this method calculates the position of the end test mass for each arm from corner station position, arm bearing, and arm length, assuming the end stations lie on a perfectly spherical earth, as the earth is assumed in the model in the absence of tidal forces. This gives us three points on the earth's surface all at the radius of the corner station in terms of latitude and longitude coordinates. I henceforth refer to the displacement vector from the corner station to a given end station as **L**, as in figure 2, in cartesian coordinates.

We will now consider only one arm at a time, as the calculations for each arm are independent. First, we displace each point according to the equations presented in the previous section, employing the potential from section 2.1 in the love equations (the specific forms of the equations can be seen in section A.1). The displaced points are then converted to cartesian coordinates, and the displacement vector $\mathbf{L}'$ is computed. To get only the longitudinal displacement along the direction of the initial beam path (**L**), we want to find $|\mathbf{L}'|\cos(\theta)$, where θ is the angle between the original and final displacement vectors, or in other words, calculate the dot product of the vectors and divide by the magnitude of **L**:

$$L'_{long} = |\mathbf{L}'|\cos(\theta) = \frac{\mathbf{L}\cdot\mathbf{L}'}{|\mathbf{L}|}$$

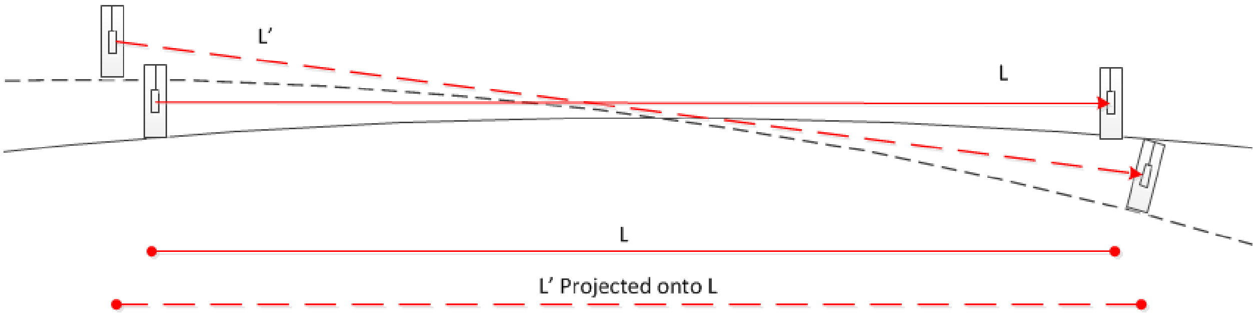

Figure 2: On the top, we see a two-dimensional diagram showing the change in the displacement vector when the mirrors move along with earth deformations; the solid line is the original position on a non-deformed earth, and the dashed line is the deformed configuration. Below we see this situation projected only along the dimension we are concerned with. The top and bottom are drawn to scale with respect to each other, and we see that the projection of **L**′ is shorter than its original length.

The deformation of a given arm is then:

$$\Delta L_{arm} = L'_{long} - |L|$$

Thus we obtain a prediction for the arm length deformation only along the beam path. This method is computationally simple, but may suffer from possible error propagation, due to multiple steps involved, and due to the estimation of end station position, as opposed to requiring an independent input of all three relevant test mass positions.

2.4 Strain Method

The strain method extends the love parameterization an additional step by computing the strain tensor associated with the displacement vector, and then projecting the longitudinal components of this strain (the diagonal matrix elements) along the length of an interferometer arm, assuming strain is relatively unchanged and the arm lies in an approximately Cartesian plane[9]. This method is computationally complex but requires a minimum of input parameters, just corner station location, arm length, and arm bearing, on top of the positional data required for both methods. The computation of the strain tensor however introduces a further unknown, which Melchior[9] calls η:

$$\eta = a\left(\frac{\partial h(r)}{\partial r}\right)\bigg|_a - 2h$$

Melchior[9] cites this new value to be $\eta \approx -0.25$. This however is a third parameter of the model which incorporates a much less testable constant, that is the instantaneous rate of change of h with height.

I discuss in more detail the strain method of deformation calculation in the first progress report[11]; additional discussion, description, and derivation can be found in topical works by Melchior[9] and Agnew[10]. See section A.2 for specific forms used and a brief summary.

2.5 Comparison of Methods

I described each deformation calculation method above, pointing out some of the advantages and disadvantages of each as I did so. Comparing them directly, we can note a few difference which might make one method more preferable than the other, given a specific situation. I mentioned that the displacement method might suffer from high degree of error propagation and accuracy concerns. This is due mainly to the fact that we compute two vectors on the order of a few kilometers in magnitude, and then attempt to compute a deformation on the order of a few micrometers, testing the limits of accuracy of some basic approximations used for the calculations; additionally, it requires the computation of end station location, which is non-trivial given the spherical geometry of the earth, a non-negligible factor in the position calculation.

If accuracy of computation can be trusted completely, the displacement method is much preferable to the strain method, which, on top of adding additional model uncertainty in the form of an extra parameter, makes use of a few assumptions which may not necessarily hold over the length of the interferometer arms. Specifically, the strain method assumes that the strain is constant over the 4km length of an arm and the only source of longitudinal displacement is from ground deformation (the vertical deformation does not contribute). While these assumptions are valid for a true strain measurement, using devices on the order of a few centimeters, their validity can certainly be questioned for use on a 4km baseline. Determination of which method should be used will inevitably be decided as the models are tested and validated; as described in sections 3.1 and 3.3, both are currently employed in parallel by the prediction code, and are present in the EPICS system.

2.6 Common and Differential Modes

Using the model presented above, we can predict the magnitude and time dependence of the tidal effects on each of the arms of the interferometer. There is a more convenient basis for expressing these tidal deformations however, as it is more beneficial to make smaller adjustments in a variety of ways, as opposed to trying to lengthen or shrink the arms by the full extent of the tidal displacement. Instead of discussing deformation per arm, we calculate quantities called differential and common mode deformation; these are quantities common to control systems in which one effect may alter a variety of variables in various ways, and merely means we will separate the tidal components which act constructively from those that act destructively[1;6]; it can be thought of as expressing the effects in a space defined by laser frequency as well as arm length, which allows us greater freedom of movement within the space.

In our case, we define common mode ΔL^{+} deformation as the mean of the deformation on each arm, and differential mode ΔL^{-} deformation as the difference between the deformations on each arm:

$$\Delta L^{+} = \frac{\Delta Y + \Delta X}{2} \tag{1}$$

$$\Delta L^{-} = \frac{\Delta Y - \Delta X}{2} \tag{2}$$

where ΔY and ΔX are the deformations on the Y and X arms, respectively. Thus we can see that if both arms are stretched by the same amount, only common mode deformation will increase, and if they are stretched equally and in opposite directions, only the differential mode deformation will increase. These definitions are merely used for convenience; they provide advantages over the use of individual arm deformations that arise from our particular situation, which I will discuss in more detail when I discuss noise suppression and tidal compensation in section 4.

3 Tidal Prediction

The utility of having the analytic model described in the previous section is that we can use it to predict the tidal deformation of the interferometer at any given time, provided we know the corner station location, arm bearings, and the position of the moon and sun relative to the earth at a given time. In this section, I describe the prediction program created to evaluate these models and construct time series of tidal deformation expectations, analyze the resulting predictions, and discuss the integration of this prediction system into the data storage system alongside the signals generated by the interferometer.

3.1 Prediction Program

As a first step to determining how best to compensate for tidal effects, I have created a tidal prediction code, which uses the models from section 2 to predict how tidal deformations change over a given time period. The program can employ one or both of the methods I have described, and in the rest of this paper I discuss both methods at every step. The program has also been generalized to apply to any of the aLIGO sites, and may be easily ported for use at Livingston or in the future India facility; in addition, preliminary support for GEO, VIRGO, and KAGRA has been added, although arm length for a given site has not been taken into account for the calculations.

The program has been written in C, and employs command line arguments to specify prediction time range, and environment variables to specify site, prediction mode, and other relevant settings. I describe an earlier version of the program in detail in Kurinsky[11], and refer the reader there for information about the internal structure of the program and details on its invocation; additionally, more information can be found on the Tidal Prediction aWiki page[12].

3.2 aLIGO Tidal Signals

Using this tidal prediction program, I have generated predictions for timescales of one day, two months, and ten years, and have plotted the daily and monthly tides, as well as a power spectrum computed using the ten-year predictions; these can be seen in figures 3, 4, and 5.

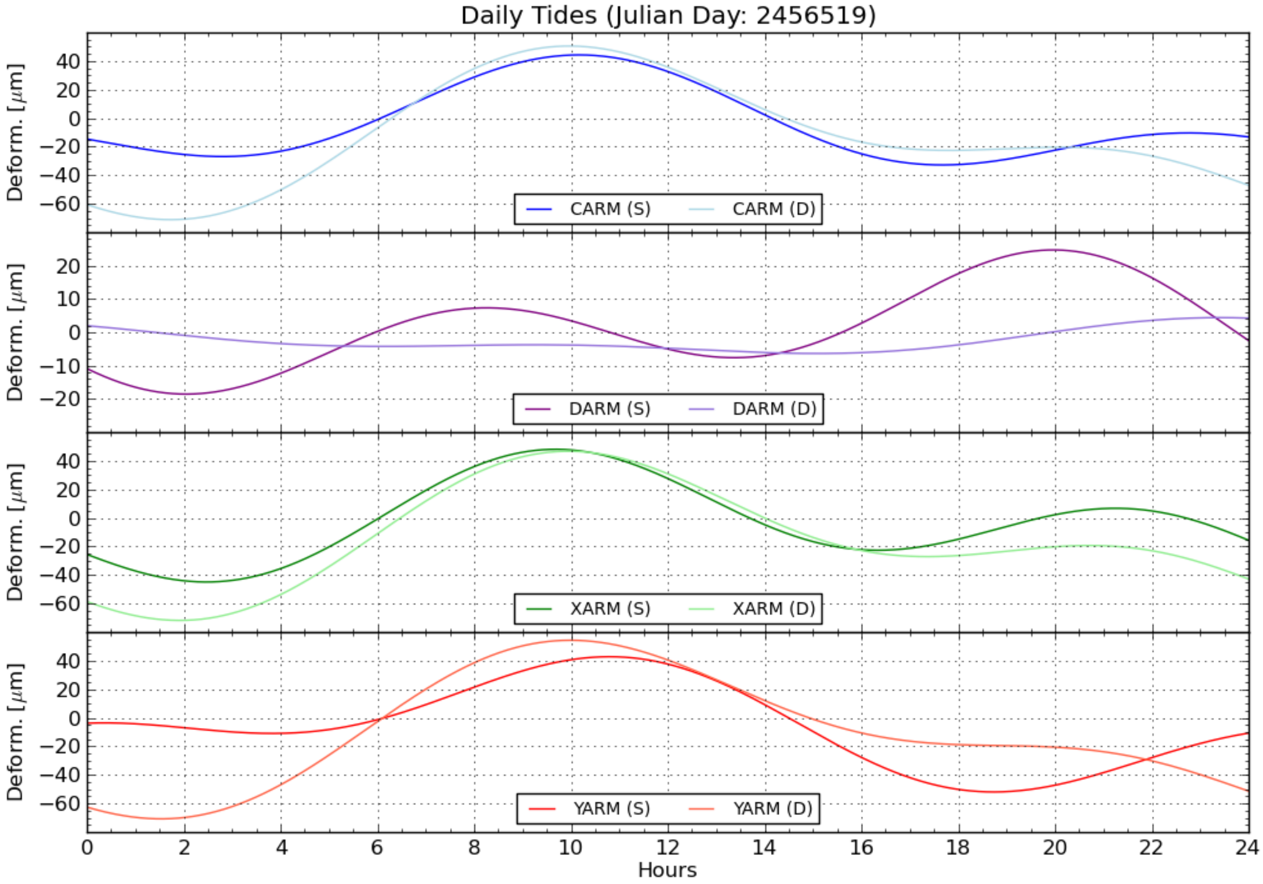

Figure 3: Graph of tidal deformations for an average 24 hour period, using both calculation methods.

In the daily spectrum, we can see both the daily and twice daily tidal components, and also not some similarities and discrepancies between the two prediction methods. Towards the middle of the day, the X arm and the common mode signals are almost exactly the same for each model, while the differential mode signal is discrepant over the entirety of the time range, and the Y arm's agreement between models is tenuous at best.

Turning to the monthly plot, we can note a few more discrepancies. The differential mode deformation seems to vary between prediction methods only in overall magnitude, however the arm and common mode deformations are of much larger magnitude and seem to carry a slightly different time dependence, possibly due to the fact that one method takes into account spatial effects (the external body's position is dependent on corner and end station location) whereas one does not. This is one aspect of the models which should be relatively easy to test through comparison to real data, when it can be made available. From a preliminary check by eye from a similar plot in Adhikari[6], it would seem that this does not happen, although that analysis was performed using LLO data whereas these are predictions for the LHO interferometer.

In the monthly plot we also notice that the common mode signal is much greater for the displace-

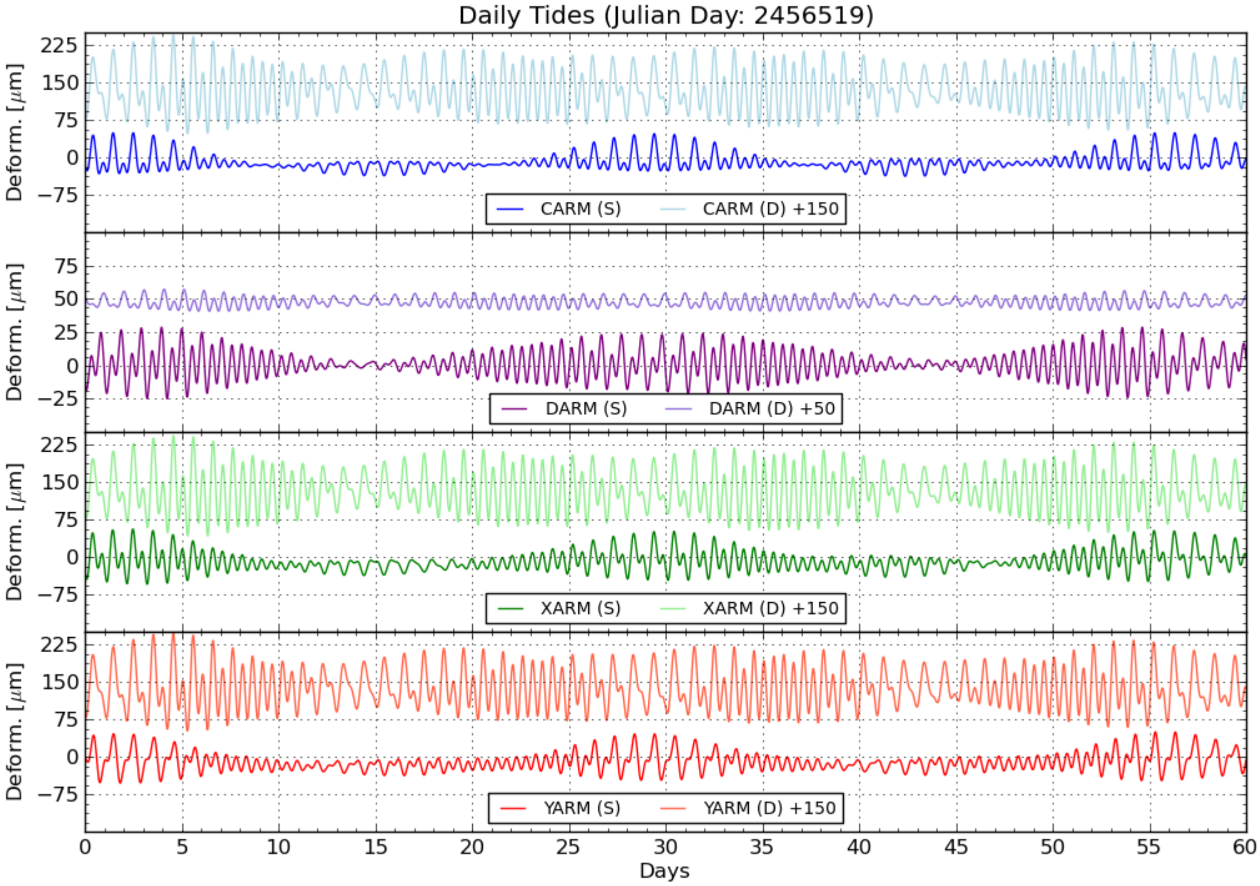

Figure 4: Graph of tidal deformations for a 60 day period using both computation methods, illustrating the effect of lunar cycles on tidal deformation. Displacement predictions are offset from 0 by a constant for convenience of comparison.

ment prediction method than the strain method, and the opposite is true of the differential mode signal. My hypothesis is that this is due to coupling of radial displacement to longitudinal deformation, however this has yet to be tested. The discrepancies lead in any case to the conclusion that in order to trust either model, some sort of comparison to real data is required, which at the moment is unavailable due to the early stage in commissioning during which this project was performed; I will discuss validation issues in more detail in section 5.

The real take away from these two plots is that, if we were to make a numerical model for a given day, we could use a model consisting of the sum of a once daily and twice daily sine wave, and fit parameters controlling the relative magnitude of these waves as well as the overall magnitude of the tidal effect. The only true unknown, discrepant aspect of this model is in fact the time dependence of the coefficients of these waves; the daily periodicity of the waves is the same for both models.

Extending this thought process to a tidal frequency analysis, we can see the range of frequencies at which tidal deformations are to be found in figure 5. This gives us a decent idea of the frequency

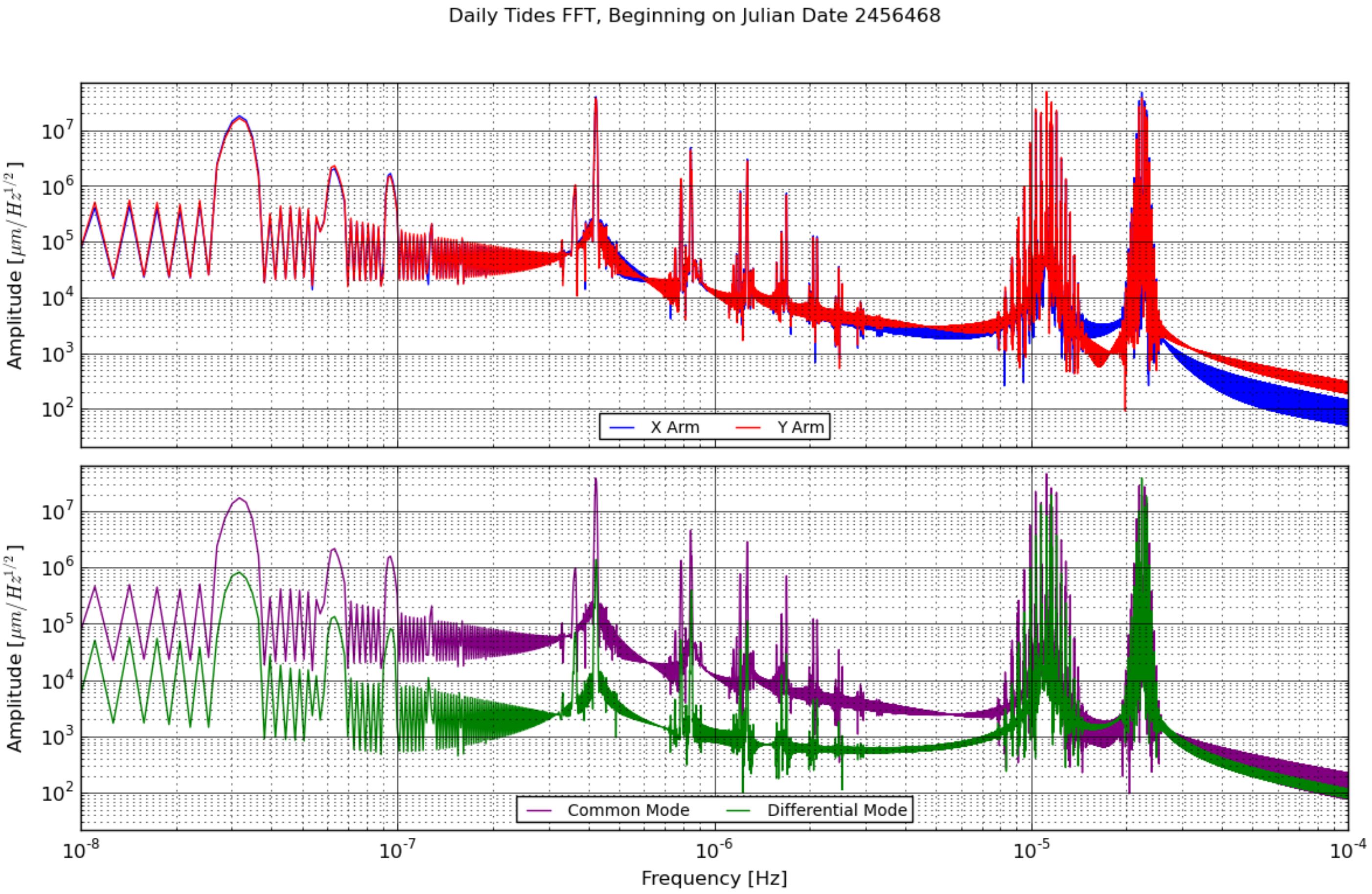

Figure 5: Power spectrum of the tidal displacements, using predictions over a ten-year time-scale. Here we see well defined peaks for daily and twice daily fluctuations, as well as various monthly harmonics from lunar motion (solar harmonics also occur at lower frequencies).

range we must analyze in determining how well tidal effects can be removed through various compensation schemes. Here we can see the various daily and twice daily modes, as well as frequencies derived from lunar position variation; solar variations are too low frequency to be seen in this particular plot, and in any case are much weaker than solar harmonics, which dominate the magnitude of the tidal effects.

3.3 EPICS Integration

The tidal prediction program in its current form has also been coded into a device support module for EPICS, and is capable of running continuously, generating predictions for the x arm, y arm, common and differential mode deformations predicted by each method given current system time. In the present form the program can mainly be used as a monitor, and can easily be compared to other interferometer signals with the various data analysis tools found on the control room computers. The signals themselves have been given the tag `H0:PEM-TIDAL`, followed by the method used (`_STRAIN or _DISP`) and then the signal (`_CARM,_DARM,_YARM, or _XARM`). For more details on the implementation and functionality of this epics module, see appendix section B. Much of this information can also be found on the Tidal Prediction aWiki page.

4 Tidal Suppression in aLIGO

I described in the introduction how many different systems exist to combat various types of experimental noise, and the importance of such systems for the sensitivity of aLIGO. In many aLIGO sensitivity analyses (such as those in Adhikari[6]) only the 1-10^5 Hz range is analyzed, as this is the frequency regime of in which the aLIGO interferometers are capable of detecting gravitational waves and thus the regime in which highest sensitivity is required. In this regime, there are many systems, including the immensely complex passive and active suspension systems, which work to filter out various sources of noise arising from seismic and thermal origins[1;6].

At the ultra-low frequencies of the tidal effects, there is only the active portion of the Length Sensing and Control (LSC[13]) system, which is responsible for maintaining the interferometer in a null, stationary state. In this section, I will briefly outline the control scheme employed by the LSC system through which tidal effects would be felt, and then analyze the ability of the LSC system to compensate for tidal effects in light of the prediction from the previous section. I will then describe the modifications which will be necessary to ensure tidal effects are properly removed from the interferometer.

4.1 Length Sensing and Control (LSC)

A schematic diagram of the components of the LSC signal paths sensitive to near-DC effects can be seen in figure 6. Looking at this diagram, it becomes clear why earlier I opted to introduce common and differential mode signals instead of using solely arm deformations; these are signals which naturally emerge from different portions of a Michelson interferometer.

The differential mode loop exists at the ”dark” port, or the traditional output of the interferometer, and the deviation of the interferometer from the operating point is determined by a DC readout method[14]. In essence, this entails monitoring the fraction of laser power which travels from the input of the interferometer to its output, and in the absence of any sort of signal (in the null state) the difference between this level and the selected operating point is zero; In other words, how far the phase difference between the incoming beams is from the desired phase difference.

The differential mode control scheme is thus to extract the difference of normalized output power from the operating point, find the deviation from the operating point, and adjust the end test masses accordingly and in opposite directions. We select a non-zero operating point in order to linearize this error signal, which allows for determination of the sign of the compensation signal.

The common mode loop is far more complicated, as it has more jobs than merely compensating for arm length error. Error signals in the common mode loop are obtained through RF methods (specifically, the PDH locking method[15]), and there are three in total: one at the symmetric port (after the input mode cleaner or IMC), one measuring distance from resonance of the IMC itself, and one measuring distance from resonance of the main laser from a high-finesse optical reference cavity.

Essentially, the common mode error signal (the first of the three) causes the IMC to be lengthened

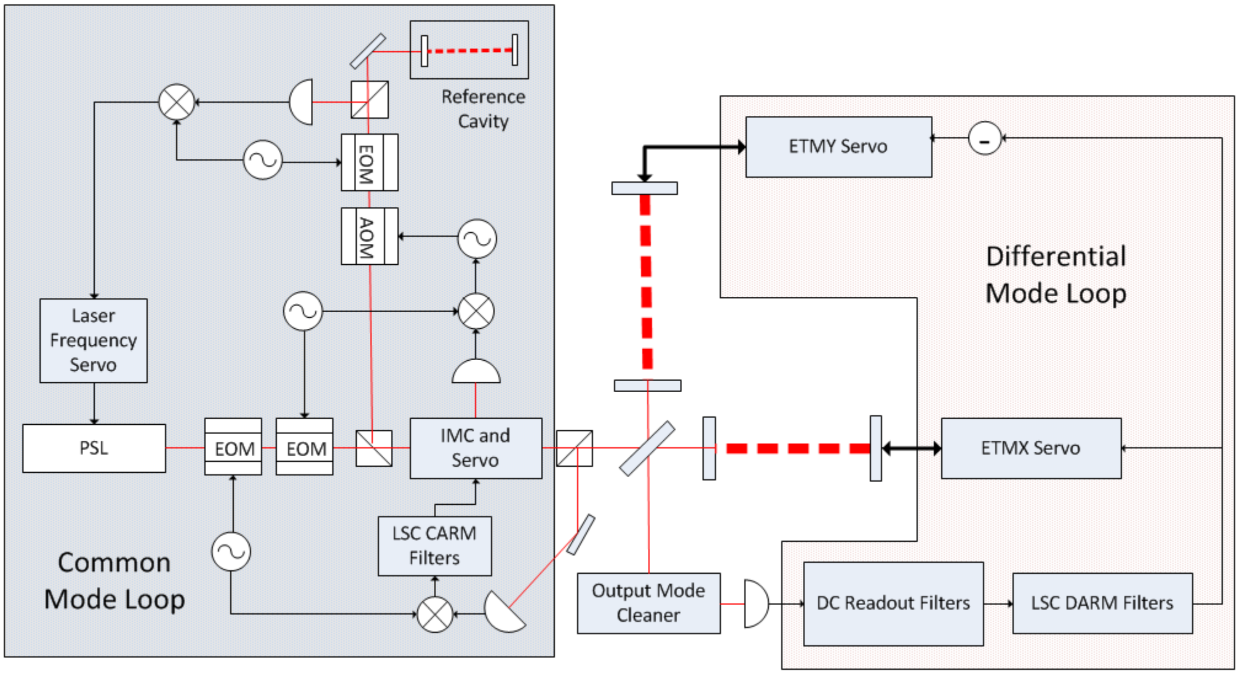

Figure 6: A schematic diagram of the LSC system, showing only paths that would allow near-DC effects such as tidal effects to propagate (here I exclude only one path with a high-pass filter, and do not show the Power Recycling and Signal Recycling cavities for the sake of simplicity). Here the reader can see the common mode compensation portion on the left, and the differential mode compensation towards the bottom right; it should be noted that the differential mode segment will also be responsible for registering gravitational wave events.

or shortened to accommodate a slightly different resonant laser frequency, which in turn causes the laser to adopt this new frequency as the carrier frequency. The reference cavity's main function is to clean the laser in the frequency domain, although temperature changes of the reference cavity will change its resonant frequency slightly and passively add to or reduce common mode error (this correlation is discussed in Kurinsky[16]).

In this way the LSC system is able to separately determine common and differential mode deformations and compensate them separately, and thus we will be able to use the prediction common and differential tidal deformations to evaluate the ability of this system to counteract tidal effects.

4.2 Evaluating LSC Tidal Compensation

Referring back to the predictions presented in section 3.2, we adopted what we considered a "worst case" tidal effect to use as the test case when analyzing LSC response to a tidal signal. This worst case effect was determined to be a peak-to-peak variation of 300 microns in a twelve hour period for the common mode loop, and 100 microns in a twelve hour period for the differential mode loop. These estimates represent about twice the magnitude of even the largest predictions and thus provide a decent buffer for the real signals; if the LSC loops can handle such a signal, they should have no problem handling tidal deformation.

4.2.1 Differential Mode Compensation

We first analyze the differential mode path in figure 6 for both frequency response and magnitude limitations. The DC readout is not frequency dependent, and all signal path filters are low pass filters with poles much higher than any frequency of interest. The DARM filter and servo path is not as simple, however the analysis of the same path during ALS characterization in Kurinsky[16] showed that this path is stable over all frequencies of interest; in addition, the end test mass actuators have a range of 1000 microns, thus the differential mode loop passes both tests of tidal compensation adequacy.

4.2.2 Common Mode Compensation

The common mode compensation path seems more complex on its face, however we can make some simplifying assumptions which reduce the analysis to a simple back of the envelope calculation. First, the PDH method has no limitations in frequency or magnitude domain with respect to tidal effects, and thus the three error signals are unbiased. We can also safely assume that the IMC and reference cavity are responsive over the entire tunable range of the PSL, which in turn can be made to initially resonate for length variations of much larger magnitude than tidal effects. These are reasonable assumptions which match design goals.

This reduces the problem to determining how well the frequency of the laser may be adjusted. This is limited by the tunable range of the VCO controlling the AOM adjacent to the reference cavity; the range for this VCO is approximately 2 MHz. This is the limiting criterion as this error signal forces the laser frequency to follow changes in the input mode cleaner through the IMC error signal. This is also the component with the smallest dynamic range.

If the interferometer is to remain in lock, it must resonate at the same mode, and thus the required change in PSL frequency to compensate for a 300 micron tidal deformation is given by

$$\Delta f = f\left(1 - \frac{L}{L + \Delta L}\right) \approx 23\,\mathrm{MHz}$$

where $f \approx 285$ THz, the PSL frequency. This is an order of magnitude larger than VCO adjustable frequency range, and thus the common mode loop as it exists currently will be quickly saturated by tidal deformation.

Despite the magnitude inadequacy, it should be noted that the common mode loop does not have any frequency limitations, as its filters and transfer functions are flat at the frequencies of interest.

4.3 Proposed LSC Modifications

In light of the previous section, we propose that the LSC be modified with an additional control loop capable of offloading tidal deformations to the end test mass actuators, which, as discussed for the differential mode, are more than adequate to handle any of the predicted tidal signals. This additional loop should consist of a low pass filter with a pole around 1 mHz, and a gain much larger than the common mode loop at low frequency such that at the frequencies of interest, the new loop dominates the feedback mechanisms. This proposed loop can be seen in figure 7.

The commissioning of such a loop would entail characterizing the crossover between the existing and proposed loops, and verifying that no other ultra-low frequency signals exist near the crossover

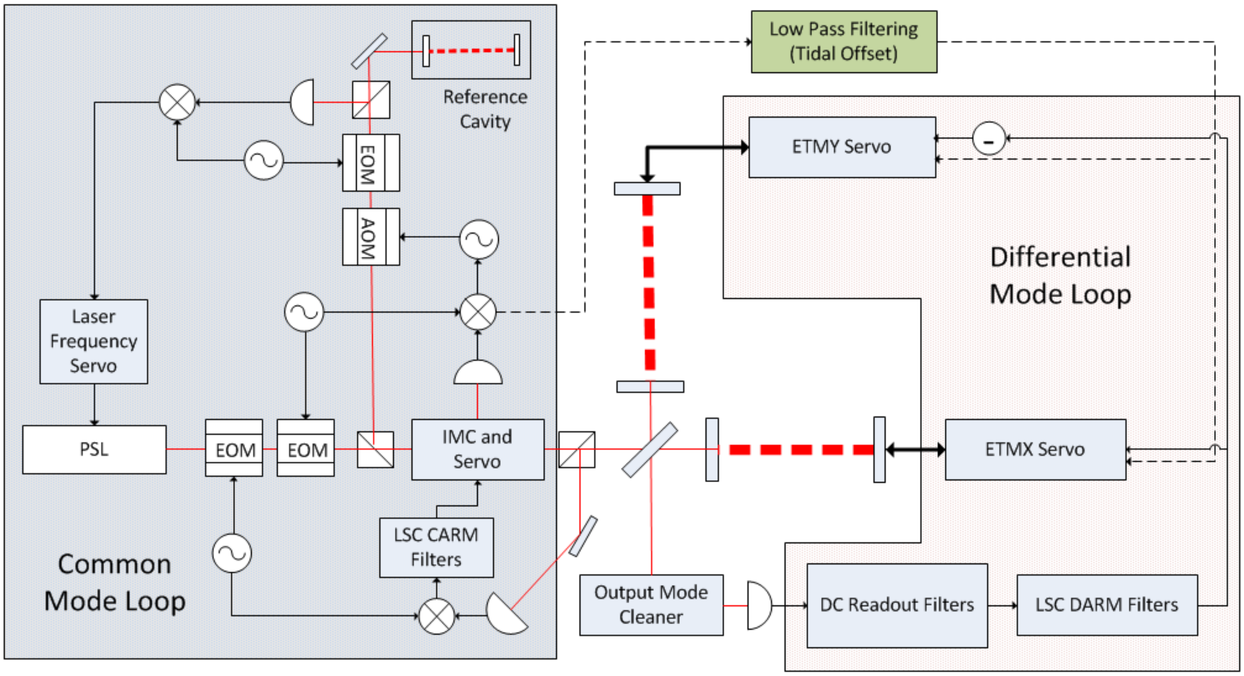

Figure 7: LSC system with the addition of the proposed control signal.

which may lead to a control systems instability, but in principle this loop should be able to offload tidal effects successfully, as none of the existing hardware preclude such a loop from being successful.

5 Initial Results and Validation

The largest problem faced during this project was the lack of available data capable of being used to validate the prediction models or test the long-term stability of the current offloading scheme. Early on, I attempted to use locking data obtained during the half interferometer test[17] to see if the end test mass drift matched predictions, however the lack of active compensation for temperature related PSL frequency shifts made the locks unstable, and therefore no lock lasted long enough or was stable enough to produce data useful for this purpose[16]. A short attempt to use data from the sixth science run of LIGO was also made, however we were unable to determine a time range corresponding to a lock of sufficient duration for testing.

The LSC system was completely unavailable for testing for much the same reason, as it relies on the interferometer outputs which an nonexistent in the absence of two fully functional arms. The infrastructure for the system is setup, however, so the frequency and magnitude analysis was largely based on actual data; other outstanding questions will naturally be solved during LSC testing when both arms are operational, at which point the models may also be tested.

Due to these reasons, the majority of the validation efforts are left to a future project at a later step in the commissioning process. The various efforts I made can be read about in more detail in Kurinsky[11] [16], and details of steps I think should be taken in the future are discussed in section 7.

6 Conclusion

The solid earth tides introduce long period noise into the interferometer at a magnitude which ensures that, without proper compensation, longterm locking will be impossible. I have conducted and presented a thorough analysis of the basic theory of earth tides, as it applies to aLIGO, in this paper and my previous reports[11;16;18] and have produced a standalone prediction code capable of predicting this effect in real time through two distinctly different approaches.

The main goal of this project was to determine whether we could correct for tidal effects through feedback mechanisms, or whether a feedforward system was necessary to remove the predicted effects. Through analysis of both the ALS and LSC systems, we have determined that a simple modification to the current feedback scheme is all that is necessary to effective compensate for tidal effects.

In order facilitate future use of the prediction code and allow operators to monitor tidal predictions, I have integrated the prediction program into the existing control system. The prediction code runs continuously, and computes the four signals by both methods, with each having an associated EPICS signal. The thought behind this was that, during operation, tidal predictions may either be monitored, or can be checked to see if they are correlated with loss of lock. In addition, if at a future time it is determined that a feed-forward system is necessary, implementation of this system will be relatively straightforward on the prediction end.

From the information presented earlier in this paper, it is clear that the prediction code is not complete, as the validation has yet to be performed, and the LSC modification must also be implemented. I have provided details of a few future efforts which I believe to be worthwhile in the following section.

7 Future Directions

Following from this work and the decisions made herein, there are a few areas which should be revisited as the commissioning process of aLIGO comes closer to completion. First, and most importantly, the proposed LSC modification should be reviewed, and if approved should be designed, characterized, implemented, and tested, such that long-term lock is indeed possible. Additionally, with this system in place, the predictions should be compared to observed DC LSC control signals to determine which model is more accurate, if either. Additionally, the models should be able to account for drifts seen in initial and enhanced LIGO, and predictions should be compared to past data as well.

At the very least, even without validation, the current predictions should be at least a good indication of the time dependence of tidal effects and general daily strength, only discrepant from true tides by relative contribution of daily and twice daily tides. Any small discrepancies could possibly be resolved by further refinement of input parameters, specifically position of the corner station and arm bearing, as there have a large effect on the prediction due to the directional nature of the tidal effects.

Acknowledgements: I would like to thank Kiwamu Izumi for all he taught me during the course of this project and for his mentorship, and Keita Kawabe for his help for the week that Kiwamu was away. I would also like to thank Dave Barker and Patrick Thomas for their help in integrating the prediction code into the EPICS system. This work was made possible by the efforts of those at the USNO, who developed the NOVAS libraries, and those at JPL who developed and packaged the high-precision ephemeris used to predict the location of the moon and sun.

References

[1] P.R. Saulson. *Fundamentals of Interferometric Gravitational Wave Detectors*. World Scientific, 1994. ISBN 9789810218201.

[2] Alex Abramovici, William E. Althouse, Ronald W. P. Drever, Yekta Grsel, Seiji Kawamura, Frederick J. Raab, David Shoemaker, Lisa Sievers, Robert E. Spero, Kip S. Thorne, Rochus E. Vogt, Rainer Weiss, Stanley E. Whitcomb, and Michael E. Zucker. LIGO: The Laser Interferometer Gravitational-Wave Observatory. *Science*, 256(5055):325–333, 1992. doi: 10.1126/science.256.5055.325. URL `http://www.sciencemag.org/content/256/5055/325.abstract`.

[3] B.S. Sathyaprakash and Bernard F. Schutz. Physics, Astrophysics and Cosmology with Gravitational Waves. *Living Reviews in Relativity*, 12(2), 2009. doi: 10.12942/lrr-2009-2. URL `http://www.livingreviews.org/lrr-2009-2`.

[4] P. Fritschel. Second generation instruments for the Laser Interferometer Gravitational Wave Observatory (LIGO). In M. Cruise and P. Saulson, editors, *Society of Photo-Optical Instrumentation Engineers (SPIE) Conference Series*, volume 4856 of *Society of Photo-Optical Instrumentation Engineers (SPIE) Conference Series*, pages 282–291, March 2003. doi: 10.1117/12.459090.

[5] F. Raab and M. Fine. The Effect of Earth Tides on LIGO Interferometers. Technical Report LIGO-T970059-01, Laser Interferometer Gravitational Wave Observatory (LIGO), February 1997. URL `http://www.ligo-wa.caltech.edu/ligo_science/earth_tides.pdf`.

[6] Rana Adhikari. *Sensitivity and Noise Analysis of 4 km Laser Interferometric Gravitational Wave Antennae*. PhD thesis, Massachusetts Institute of Technology, July 2004. URL `https://dcc.ligo.org/LIGO-P040032`.

[7] John Bechhoefer. Feedback for physicists: A tutorial essay on control. *Rev. Mod. Phys.*, 77:783–836, Aug 2005. doi: 10.1103/RevModPhys.77.783. URL `http://link.aps.org/doi/10.1103/RevModPhys.77.783`.

[8] Eric Morganson. Developing an Earth-Tides Model for LIGO Interferometers. Technical Report T990181-00, Laser Interferometer Gravitational Wave Observatory (LIGO), October 1999. URL `https://dcc.ligo.org/LIGO-T990181`.

[9] Paul Melchior. Earth Tides. *Geophysical surveys*, 1(3):275–303, 1974. ISSN 0046-5763. doi: 10.1007/BF01449116. URL `http://dx.doi.org/10.1007/BF01449116`.

[10] D. C. Agnew. *Earth Tides*, chapter 3.06. Elsevier B.V., 2007. URL `http://www.gps.caltech.edu/classes/ge167/file/agnew_treat_tide.pdf`.

[11] Noah Kurinsky. Tidal Prediction and Compensation for Advanced LIGO: First Progress Report. Technical Report LIGO-T1300601-v1, Laser Interferometer Gravitational Wave Observatory (LIGO), July 2013. URL `https://dcc.ligo.org/LIGO-T1300601-v1`.

[12] aLIGO Tidal Wiki Page. `https://awiki.ligo-wa.caltech.edu/aLIGO/Tidal%20Prediction`. Accessed: 2013-08-31.

[13] R. Abbot, R. Adhikari, S. Ballmer, L. Barsotti, M. Evans, Frolov V. Fritschel, P., G. Mueller, B. Slagmolen, S. Waldman, and et. al. Advanced LIGO Length Sensing and Control Final Design. Technical Report LIGO-T1000298-v2, Laser Interferometer Gravitational Wave Observatory (LIGO), June 2010. URL `https://dcc.ligo.org/LIGO-T1000298-v2`.

[14] S. Hild, H. Grote, S. Degallaix, J.and Chelkowski, K. Danzmann, A. Freise, M. Hewitson, J. Hough,

H. Luck, M. Prijatelj, K.A. Strain, J.R. Smith, and B. Wilke. DC-readout of a Signal-Recycled gravitational wave detector. 2008.

[15] Eric D. Black. An Introduction to Pound-Drever-Hall Laser Frequency Stabilization. Technical Report LIGO-P990042, Laser Interferometer Gravitational Wave Observatory (LIGO), April 2000. URL `https://dcc.ligo.org/LIGO-P990042`.

[16] Noah Kurinsky. Tidal Prediction and Compensation for Advanced LIGO: Second Progress Report. Technical Report LIGO-T1300601-v2, Laser Interferometer Gravitational Wave Observatory (LIGO), August 2013. URL `https://dcc.ligo.org/LIGO-T1300601-v2`.

[17] D. Sigg, K. Kawabe, and P. Fritschel. Commissioning Advanced LIGO's HIFO-Y. Technical Report LIGO-T1300174-v2, Laser Interferometer Gravitational Wave Observatory (LIGO), March 2013. URL `https://dcc.ligo.org/LIGO-T1300174-v2`.

[18] Noah Kurinsky. Tidal Prediction and Compensation for Advanced LIGO: Project Plan. Technical Report LIGO-L1300145-v1, Laser Interferometer Gravitational Wave Observatory (LIGO), May 2013. URL `https://dcc.ligo.org/LIGO-L1300145-v1`.

[19] LHOCDS Tidal Wiki Page. `https://lhocds.ligo-wa.caltech.edu/wiki/h0tidal`. Accessed: 2013-08-31.

A Tidal Deformation Terms

This section merely serves as a reference for those interested in the analytic forms of the tidal equations as employed in the prediction program; for a strain derivation, see Melchior[9] and Raab and Fine[5]. The displacement forms should be straightforward calculations from the equations presented in the main text.

A.1 Displacement

These displacements should be added to position of the site in geocentric coordinates to get the new location of the site.

$$u_r = \frac{3hGM_O r^2}{4gd^3}\left(\cos^2(\theta)\cos^2(\delta)\cos(2H) + \sin(2\theta)\sin(2\delta)\cos(H) + 3\left(\sin^2(\theta) - \frac{1}{3}\right)\left(\sin^2(\delta) - \frac{1}{3}\right)\right)$$

$$u_\theta = \frac{3lGM_O r}{4gd^3}\left(-\sin(2\theta)\cos^2(\delta)\cos(2H) + 2\cos(2\theta)\sin(2\delta)\cos(H) + 3\sin(2\theta)\left(\sin^2(\delta) - \frac{1}{3}\right)\right)$$

$$u_\lambda = \frac{3lGM_O r}{4gd^3\cos(\theta)}\left(2\cos^2(\theta)\cos^2(\delta)\sin(2H) + \sin(2\theta)\sin(2\delta)\sin(H)\right)$$

In the above, M_O is object mass, and all other terms are as defined in the text. The units of radial displacement is meters while the other two terms are in radians.

A.2 Strain

The total strain due to a the tidal effects is the sum of three distinct strain components, a constant, daily, and twice daily term, also called the Zonal, Tesseral, and Sectorial components of the strain, respectively:

- Tesseral Strain:

$$\begin{aligned} d_T = {} & \left[\left(\eta\cos^2(z) + (h-4l)\cos^2\beta + (h-2l)\sin^2\beta\right)\cos H \right. \\ & \left. -\left(2l\frac{\cos\beta\sin\beta}{\cos\theta}\right)\sin H\right] \\ & \times\left[\frac{D}{ag}\left(\frac{r}{a}\right)^2\left(\frac{c}{d}\right)^3\sin 2\theta\sin 2\delta\right] \end{aligned}$$

- Sectorial Strain:

$$\begin{aligned} d_S = &\Big\{\Big[\eta\cos^2(z)\sin^2(\theta) \\ &+\Big(h\sin^2\theta + 2l(1-2\sin^2\theta)\Big)\cos^2\beta \\ &+\Big(h\sin^2\theta - 2l(1+sin^2\theta)\Big)\sin^2\beta\Big]\cos 2H \\ &+[(4l\cos\theta)\sin\beta\cos\beta]\sin 2H\} \\ &\times\left[\frac{D}{ag}\left(\frac{r}{a}\right)^2\left(\frac{c}{d}\right)^3\cos^2\delta\right] \end{aligned}$$

- Zonal Strain:

$$\begin{aligned} d_Z = &\Big\{\eta(\cos^2(\theta)-1/3)\cos^2(z) \\ &+\Big[h(\cos^2\theta-1/3)-2l\cos 2\theta\Big]\cos^2\beta \\ &+\Big[h(\cos^2\theta-1/3)-2l\cos^2\theta\Big]\sin^2\beta\Big\} \\ &\times\left[\frac{D}{ag}\left(\frac{r}{a}\right)^2\left(\frac{c}{d}\right)^3(\sin^2\theta-1/3)\right] \end{aligned}$$

In the above, g is the gravitational acceleration at earth's surface, c is the mean earth-body distance, a is the mean earth radius, $\theta = \pi/2 - \phi$ is the colatitude of the site, and $\cos\beta = \sin(z)\cos(\psi)$ ($\sin\beta = \sin(z)\sin(\psi)$), where ψ is the bearing of the beam in degrees ($\psi = 0$ corresponds to due north) and z is the zenith angle between the site and the object ($z = \delta - \lambda$). The rest of the variables are as defined for the potential, or are l, h, or η, the love numbers. The deformation resulting from this strain is the strain multiplied by the length of an arm.

B EPICS Integration Details

The tidal prediction code discussed in the text has been simplified and inserted into an EPICS support module, such that an IOC may use this module to produce signals readable by the LIGO EPICS related utilities. The modified program control converts current system time into Julian date, and then runs the tidal predictions by both methods, storing the results in a global structure, along with the system time. These are then readable by the IOC through a function call. The IOC in turn runs repeatedly, querying the module for updated values in regular intervals.

The signals generated by the IOC have been categorized under the Physical and Environmental Monitoring group, and have the following labels:

```
H0:PEM-TIDAL_STRAIN_CARM
H0:PEM-TIDAL_STRAIN_DARM
H0:PEM-TIDAL_STRAIN_XARM
H0:PEM-TIDAL_STRAIN_YARM
H0:PEM-TIDAL_DISP_CARM
H0:PEM-TIDAL_DISP_DARM
H0:PEM-TIDAL_DISP_XARM
H0:PEM-TIDAL_DISP_YARM
H0:PEM-TIDAL_UNIXTIME
```

These signals can be read in real time with utilities like StripTool, but are also stored in the frames and can be viewed with dataviewer; a few days of frames data from the time of this writing can be seen in figure 8. For system specific details, refer to the the Tidal Prediction aWiki page[12] and the h0tidal LHOCDS Wiki Page[19].

Despite these Hanford specific details, we have developed an IOC for livingston as well, and both the location of the ephemeris file and the site to be used for prediction are passed to the support module at startup; these are found in the IOC st.cmd file. This same infrastructure may thus easily be implemented at Livingston at a later date if desired, and India as well, with minor code modification to add site details.

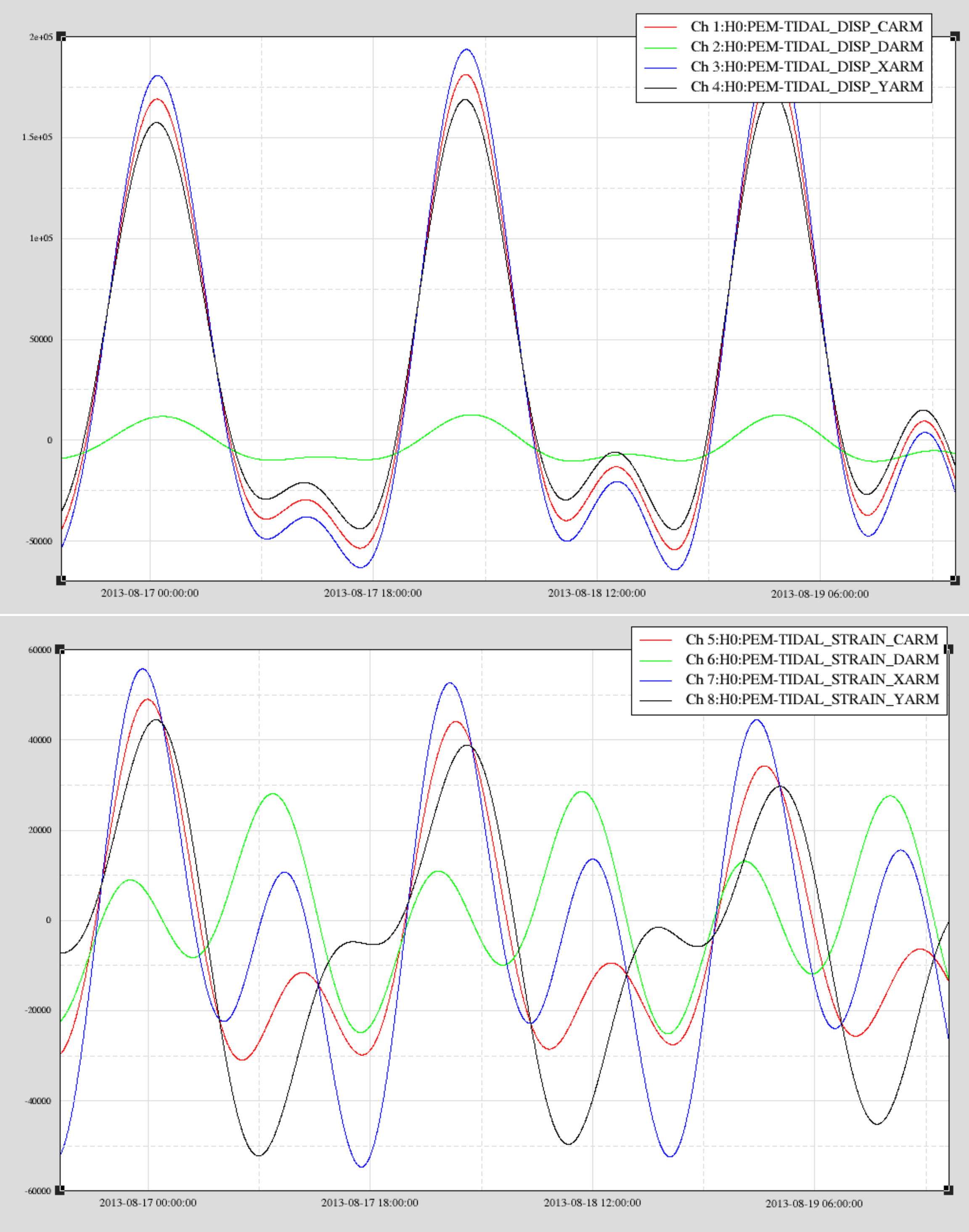

Figure 8: Example of the EPICS signals from long-term memory, displayed using dataviewer, for a three day time range.